LETTER

A universal biomolecular integral feedback controller for robust perfect adaptation

Stephanie K. Aoki[1,2], Gabriele Lillacci[1,2], Ankit Gupta[1,2], Armin Baumschlager[1], David Schweingruber[1] & Mustafa Khammash[1]*

Homeostasis is a recurring theme in biology that ensures that regulated variables robustly—and in some systems, completely— adapt to environmental perturbations. This robust perfect adaptation feature is achieved in natural circuits by using integral control, a negative feedback strategy that performs mathematical integration to achieve structurally robust regulation[1,2]. Despite its benefits, the synthetic realization of integral feedback in living cells has remained elusive owing to the complexity of the required biological computations. Here we prove mathematically that there is a single fundamental biomolecular controller topology[3] that realizes integral feedback and achieves robust perfect adaptation in arbitrary intracellular networks with noisy dynamics. This adaptation property is guaranteed both for the population-average and for the time-average of single cells. On the basis of this concept, we genetically engineer a synthetic integral feedback controller in living cells[4] and demonstrate its tunability and adaptation properties.

A growth-rate control application in *Escherichia coli* shows the intrinsic capacity of our integral controller to deliver robustness and highlights its potential use as a versatile controller for regulation of biological variables in uncertain networks. Our results provide conceptual and practical tools in the area of cybergenetics[3,5], for engineering synthetic controllers that steer the dynamics of living systems[3–9].

Integral feedback control is arguably one of the most fundamental regulation strategies in engineering practice. From modern jetliners to industrial plants, integral feedback loops reliably drive physical variables to their desired values with great robustness and precision[10]. It is increasingly appreciated that nature's evolutionary explorations had already discovered the same strategy, which has functioned at various levels of biological organization to achieve homeostasis and robust adaptation to perturbations[1,2,11–13]. Integral feedback occurs by sensing the deviation of a variable of interest (controlled variable) from the
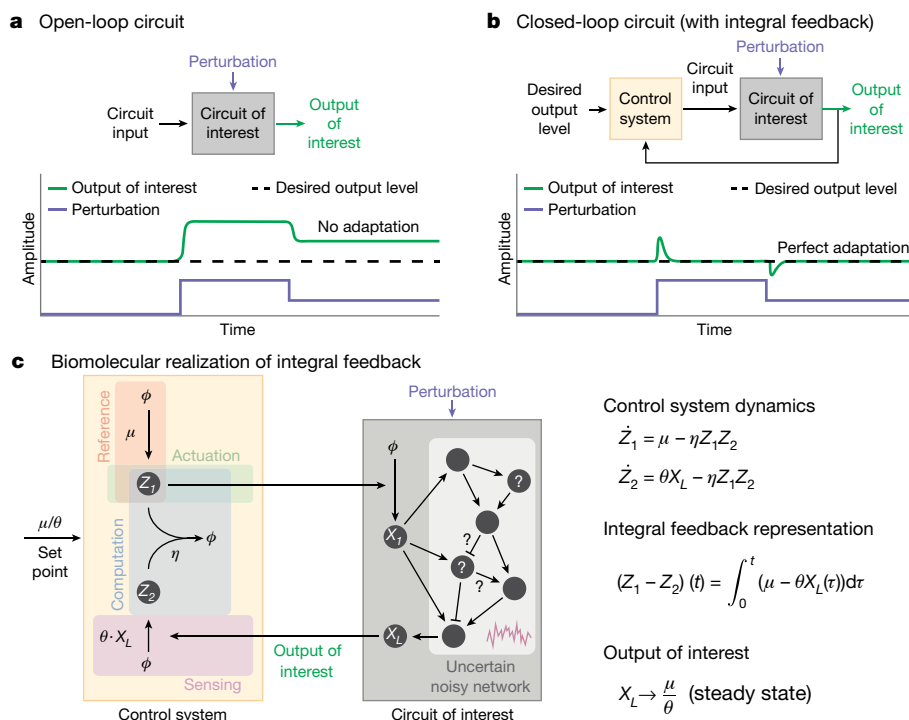

Fig. 1 | Integral feedback enables robust perfect adaptation. a, In a circuit without feedback regulation (open-loop circuit), the output is sensitive to external perturbations, which drive it away from the desired value (no adaptation). **b**, Integral feedback confers robustness to perturbations and keeps the output tightly regulated at desired levels (RPA). **c**, The antithetic integral control motif offers a biologically realizable integral feedback scheme using two regulator species. The output of interest, X_L is sensed by a reaction the product of which, Z_2, is produced at a rate proportional to X_L (rate constant θ). A reference

reaction yields Z_1 with rate constant μ. Z_1 and Z_2 annihilate (or sequester) each other, an operation that is central to the integral feedback computation. In turn, Z_1 works as an actuator by affecting processes that lead to the increase in the production of the output of interest, thereby closing the feedback loop. In this scheme, as long as the closed dynamics are stable, the steady-state value of the output is determined solely by the ratio μ/θ. Notably, it does not depend on the topology and parameters of the circuit of interest, which are usually uncertain and noisy, nor on any constant external perturbations that afflict the network.

[1]Department of Biosystems Science and Engineering, ETH Zürich, Basel, Switzerland. [2]These authors contributed equally: Stephanie K. Aoki, Gabriele Lillacci, Ankit Gupta.
*e-mail: mustafa.khammash@bsse.ethz.ch

Box 1

Universality of the antithetic feedback controller motif

Consider the problem of controlling an arbitrary biomolecular network, comprising species $X_1, …, X_N$, by connecting it with a feedback controller that is realizable as another network with species $Z_1, …, Z_C$ (a). The controlled network species can interact with the controller species via actuation reactions that do not affect the controller's state, and via a sensing reaction, which is catalysed by the output species of interest X_L and acts by producing or degrading some controller species Z_i (for example, $Z_i + X_L \rightarrow X_L$ or $X_L \rightarrow Z_i + X_L$). Additionally, there is a set-point encoding reaction that can produce or degrade some controller species Z_j. The set-point encoding reaction and the sensing reaction follow mass-action kinetics with positive rate constants μ and θ, respectively. The sensed variable is the abundance of X_L scaled multiplicatively by θ, and our control objective is to robustly steer its average value to the desired set point μ. Excluding the set-point encoding and sensing reactions, we assume that each of the remaining closed-loop network reactions depends on at least one parameter in the vector of parameters denoted by $\gamma = (\gamma_1, \gamma_2, …)$. To capture the effects of intrinsic noise, we model the reaction dynamics as a continuous-time Markov chain: $(X_\gamma(t), Z_\gamma(t))_{t \geq 0}$. The output of a single cell at time t is the random state $X_{\gamma,L}(t)$, denoting the copy number of the output species X_L, and the population-averaged output of several identical cells is given by the expectation $\mathbb{E}(X_{\gamma,L}(t))$. The controller's goal is to achieve RPA for the population average by ensuring that $\lim_{t \to \infty} \mathbb{E}(\theta X_{\gamma,L}(t)) = \mu$ holds, regardless of the initial conditions and the parameter vector γ. In other words, the population average adapts perfectly following a state perturbation or after a disturbance that alters one or more of the parameters in γ. This property also holds for the long-term average output of a single cell given by $\lim_{T \to \infty} T^{-1} \left(\int_0^T \theta X_{\gamma,L}(t) dt \right)$. We prove that all RPA-achieving controllers must have at least two species (that is, $C \geq 2$), and that the species involved in set-point encoding (say Z_1) and output sensing (say Z_2) must be distinct. We further find a linear-algebraic condition that provides a simple parameterization of all feedback controllers of any size that achieve RPA (Supplementary Text theorem 2.5). This condition can be further

unravelled to prove that each RPA-achieving controller must embed an antithetic motif. Specifically, the species set of any RPA controller can be partitioned into three disjoint subsets C_+, C_- and C_0 (b), containing species Z_1, Z_2 and the null species ϕ, respectively, and there must exist an annihilation reaction that combines a species in C_+ with one in C_- to produce a species in C_0 (shown with thick red arrows). Hence, any RPA-achieving controller can be viewed as an extension of the minimal antithetic feedback controller presented in ref. [3] (Supplementary Text section 2.2.3). Moreover, it can be shown that the class of RPA-achieving controllers in the stochastic setting is strictly contained in the class of such controllers in the deterministic setting, in which the population-averaged dynamics coincide with the single-cell dynamics (Supplementary Text section 2.2.4).
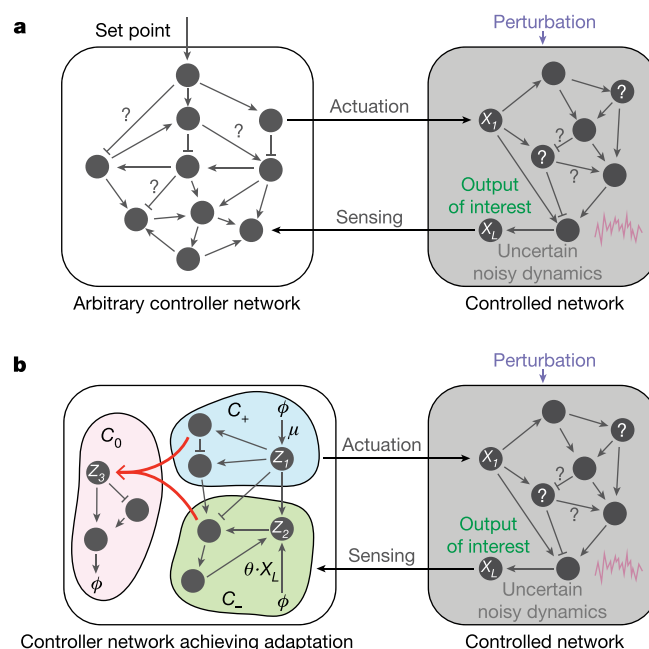
desired target value (set point), computing the mathematical integral of that deviation (error) over time, and then using it in a negative feedback configuration to drive processes that counteract the deviation and drive it to zero (Fig. 1a, b). This can be achieved despite considerable uncertainty in process dynamics and constant or slowly varying perturbations. This fundamental network property is known as robust perfect adaptation (RPA), and the importance of integral feedback as a regulation strategy derives from its capacity to realize RPA. Given the complexity of required sensing and computation (for example, subtraction, integration and so on), the in vivo synthetic implementation and demonstration of full integral feedback has remained unrealized. In a recent theoretical work[3], we introduced the antithetic feedback motif (Fig. 1c) as a network topology that realizes integral feedback while lending itself to biomolecular implementation. We showed analytically that for cells with intrinsically noisy dynamics, this regulatory motif endows the network with guaranteed robustness properties for the population average and also for the single-cell time average. This motif subtly exploits intrinsic noise, using it as a stabilization force in scenarios in which noise-free dynamics exhibit oscillations.

Consider the problem of controlling an uncertain and noisy biomolecular network by augmenting it with another feedback-controller network (see the Box 1 Figure, panel a). The control objective is to achieve RPA for some variable in the controlled network (output); that is, this variable must be steered to a desired set point and maintained

there, even in the presence of unknown constant external perturbations and in spite of uncertainty in the network topology and parameters, including the parameters of the controller network. Insisting on robustness to topology and parameters is particularly important in synthetic biology, in which the controlled network is often unknown or poorly characterized and fine-tuning the parameters of the controller network can be extremely difficult.

It is well established in control theory[14,15] that in the noise-free setting, such general-purpose controller networks must implement an integral feedback component, but designing one is challenging because of the realizability and other constraints imposed by the biomolecular reaction network[16,17]. These challenges are further amplified if we take into account the noisy nature of the intracellular dynamics, in which not all integral feedback-controller implementations lead to RPA and hence the particular topology used is critical. In this stochastic setting, when the dynamics are stable, RPA refers to the steady-state population average of the output variable or—equivalently—its long-term single-cell time average.

Given this context, several fundamental questions arise. These include how one can determine definitively whether a candidate network of any size achieves RPA in the presence of intrinsic noise; which architectural features are necessary and sufficient for a biomolecular feedback control topology to achieve RPA; whether all RPA-achieving controller topologies, regardless of their size, can be characterized; and—if the
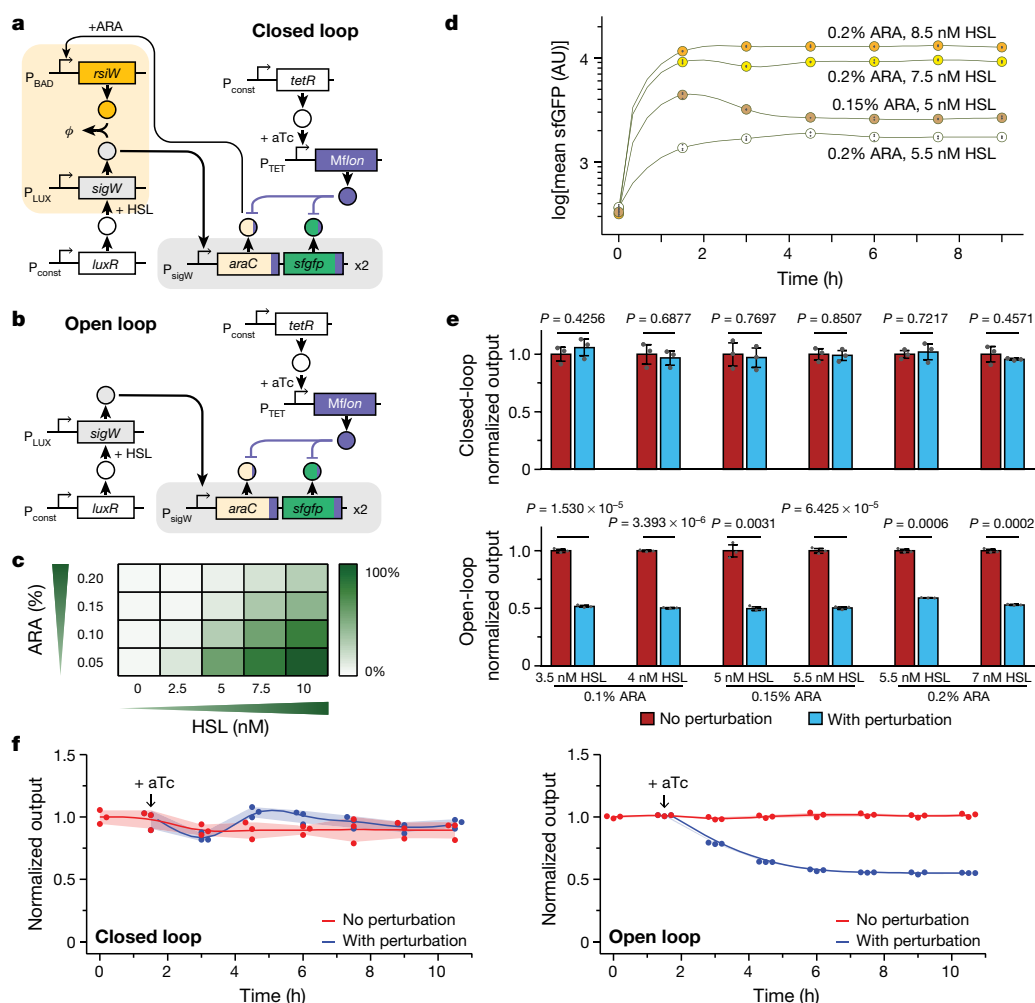
Fig. 2 | Synthetic antithetic integral feedback control circuit. a, Closed-loop circuit. The antithetic control system (beige shaded box) is tunable with HSL and ARA. The controlled circuit of interest (grey shaded box) consists of *araC* and *sfgfp* tagged with *Mf*Lon degradation tags. A negative perturbation is applied by aTc induction of M*flon* expression, resulting in AraC and sfGFP degradation. **b**, Open-loop circuit. Closed-loop feedback is disabled by deleting the anti-σ module (P$_{BAD}$-*rsiW*). **c**, Response of the closed-loop circuit to HSL and ARA. Heat map of the mean steady-state sfGFP fluorescence for corresponding concentrations of HSL and ARA normalized to the maximum output for four independent biological replicates. **d**, Dynamic response of the closed-loop circuit to HSL induction. sfGFP fluorescence is plotted as a function of time and fit with a cubic spline. Data show mean (coloured circles) ± s.d. for $n = 3$

independent biological replicates (grey dots). **e**, Output steady states of closed- and open-loop circuits in the presence of *Mf*Lon protease perturbation. sfGFP fluorescence normalized to the pre-disturbance level for each set of induction conditions. Data show mean ± s.d. for $n = 3$ independent biological replicates (grey circles). Two-tailed, unpaired, unequal variance *t*-test. Non-normalized data are shown in Extended Data Fig. 6b. **f**, Dynamic response of the closed-loop circuit to perturbation. Closed- and open-loop strains at steady state in 0.2% ARA and 5.5 nM HSL were perturbed at 1.5 h by aTc induction of *Mf*Lon expression. sfGFP fluorescence normalized to the mean at 0 h is plotted as a function of time and fit with a cubic spline for $n = 3$ independent biological replicates. Shaded regions indicate the s.d. Non-normalized data are available in Extended Data Fig. 6f.

number of species needed to implement a controller topology is used as a measure of its complexity—which controller topologies achieve RPA with minimal complexity. Here we provide definitive answers to all these questions. We prove that each RPA-achieving controller must necessarily embed the antithetic feedback motif, and thus that the antithetic feedback motif we introduced previously[3] is the minimal-complexity RPA-achieving controller for unknown networks with noisy dynamics. It is important to emphasize that these results hold only in the setting of noisy single-cell dynamics. If the network under consideration is noise-free, it is not necessary for a controller to embed antithetic feedback to achieve RPA[18–21], but it is sufficient. These results are summarized in Box 1 and the detailed proofs are in the Supplementary Text.

The original analysis of the antithetic feedback controller[3] was focused on the ideal case in which the production rates of the molecular species involved in the circuit are unsaturated, and there is negligible degradation of controller proteins Z_1 and Z_2. In living cells, these assumptions are not satisfied because all genes have a limited production capacity and, in the case of fast-growing cells, dilution of

the controller proteins must be factored into the dynamics[16]. This can introduce an error between the actual and the desired values of the controlled variable following a large disturbance. To investigate whether this error could be made small enough, we simulated a model of the antithetic motif in an *E. coli* implementation (Extended Data Figs. 1, 2, Supplementary Text section 1). Our analysis revealed that, using realistic model parameters, it is indeed possible to achieve small errors, which suggests that for all practical purposes the antithetic motif can realize perfect adaptation in growing cells.

Central to our implementation of the minimal antithetic design[3,4] are two controller proteins that annihilate (or stoichiometrically inactivate) each other; for example, by forming an inert dimer (Fig. 1c). This type of annihilation reaction has been used in existing synthetic devices[6,22], and to realize it, we used a previously reported pair of *Bacillus subtilis* σ and anti-σ factors (SigW and RsiW), which have roles in cell envelope homeostasis and display annihilation in vivo[22,23]. In its natural context, RsiW stably sequesters and holds SigW inactive[23]. Upon cell-membrane stress, RsiW is proteolytically cleaved and active SigW is released, controlling
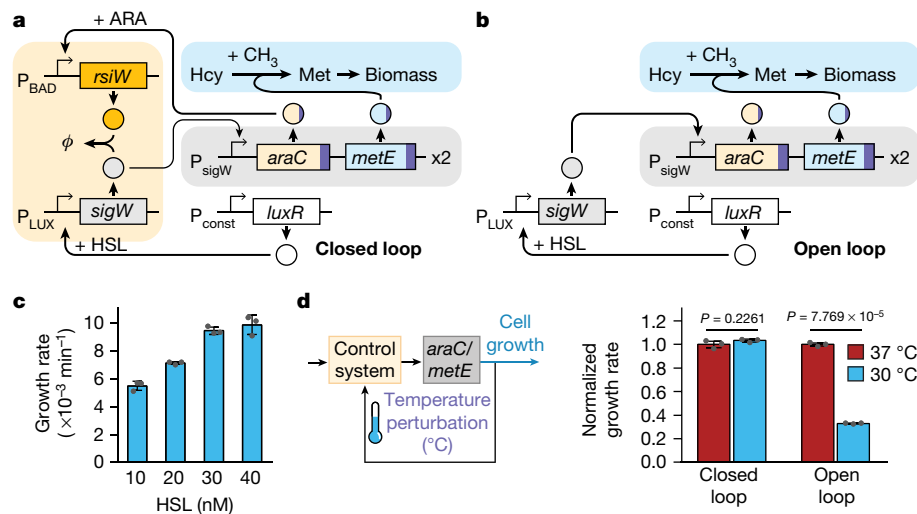
Fig. 3 | Growth-rate control. a, Closed-loop antithetic integral feedback control of growth rate. The antithetic controller (beige shaded box) controls the circuit of interest (grey shaded box), in which *sfgfp* was replaced with *metE*. MetE catalyses the last step of cobalamin-independent methionine biosynthesis by transferring a methyl group from 5-methyltetrahydropteroyl-tri-L-glutamate to L-homocysteine (Hcy, blue shaded box). **b**, Open-loop growth-control circuit. Feedback is disabled by deleting the anti-σ module (P$_{BAD}$-*rsiW*) from the closed-loop circuit. **c**, Growth rate is tunable in methionine-free medium. Steady-state growth rates of the closed-loop circuit in a Δ*metE* host strain for the corresponding concentrations of HSL and 0.2% ARA ($n = 3$).

d, Closed-loop circuit is robust to temperature perturbation. Left, a constant external change in temperature is exerted on the closed-loop circuit strain. Right, steady-state growth rates of closed- and open-loop circuits in a Δ*metE* host strain grown at 37 °C and 30 °C in methionine-free medium containing 0.2% ARA and 10 nM HSL normalized to the 37 °C rate for each circuit ($n = 3$). Two-tailed, unpaired, unequal variance *t*-test. Non-normalized data are available in Extended Data Figs. 8a, b. Data show mean ± s.d. for n independent biological replicates (grey circles in **c**, **d**). The response of the circuit to temperature perturbation at the higher set points in **c** was not characterized in this study.

expression of multiple downstream genes[23]. The high native stability of these σ and anti-σ factors enable practical realization of integral action in fast-growing cells, in contrast to RNA-based controllers[5,8,9], for which RNA instability poses a major limitation to integral action realization.

In our setup, on one plasmid SigW-responsive promoter P$_{sigW}$ drives the controlled genes, the *E. coli* transcription factor *araC* and *sfgfp* (superfolder green fluorescent protein). AraC closes the loop by regulating P$_{BAD}$ promoter-driven *rsiW* expression in a concentration-dependent manner (Fig. 2a). *sfgfp* expression should be proportional to that of *araC*, which encodes the regulated protein of interest. To mitigate saturation effects, the final plasmid contains two P$_{sigW}$-*araC*-*sfgfp* modules (Fig. 2a, Extended Data Fig. 2 and Supplementary Text). This circuit is tunable with arabinose (ARA), which increases AraC activity, and *N*-(3-oxohexanoyl)-L-homoserine lactone (HSL), which activates the constitutively expressed *Vibrio fischeri* quorum-sensing-pathway transcription factor LuxR to induce *sigW* expression driven by the *lux* promoter (P$_{LUX}$). For comparison, an open-loop control circuit was constructed without P$_{BAD}$-*rsiW* to disable feedback (Fig. 2b).

Testing of the closed-loop circuit shows that steady-state sfGFP levels can be adjusted with ARA and HSL by independently tuning *sigW* and *rsiW* expression (Fig. 2c), consistent with our theory and with recent work[3,24]. Increasing SigW production resulted in a corresponding increase in steady-state sfGFP with HSL between 0 and 10 nM, whereas increasing RsiW production with ARA between 0.05% and 0.2% corresponded to a decrease in sfGFP. Dynamic time courses of closed-loop cells precultured in ARA and induced with HSL show unimodal fluorescence detectable over background and stable over long periods of time (Fig. 2d, Extended Data Fig. 3). Further, using cell growth rate as a burden indicator[7], in the conditions tested, differences in growth rates between set points or over time were insignificant (Extended Data Fig. 4).

To test the response of the system to a constant perturbation, on a separate plasmid we used the orthogonal *Mesoplasma florum* protease Lon (*Mf*Lon)[25], driven by an anhydrotetracycline (aTc)-inducible promoter (P$_{TET}$, Fig. 2a, b). *Mf*Lon recognizes cognate Pdt degradation tags[25] appended to the C termini of AraC and sfGFP and increases protein degradation (Extended Data Fig. 5, Methods). Steady-state

sfGFP levels of both circuits with and without *Mf*Lon induction were measured and disturbance rejection was quantified as the relative output decrease post-disturbance. For multiple ARA and HSL conditions, the closed loop showed virtually no change in fluorescence after protease induction, whereas the open loop showed greater than 40% decrease in most conditions tested and neither circuit showed significant burden owing to protease induction (Fig. 2e, Extended Data Fig. 4). Dynamically, the closed loop adapts post-perturbation after a short transient (Fig. 2f, Extended Data Fig. 4). These results suggest that the closed loop is able to sense and compensate for AraC loss despite the continued presence of the perturbation, unlike the open loop. We further found that adaptation was maintained when decreasing HSL, increasing ARA or increasing both HSL and ARA from these conditions (Extended Data Fig. 6). However, increasing HSL and reducing ARA eventually leads to discernible error (though always smaller than the open-loop error), which indicates an exit from the adaptation region—as qualitatively predicted by the simulations (Extended Data Fig. 6). The observed conditions in which perfect adaptation to the *Mf*Lon disturbance is achieved were limited to an approximately three-fold output range (Extended Data Fig. 6), although the closed-loop circuit is capable of reaching higher set points in the absence of this disturbance. Moreover, the closed loop tended to show increased cell-to-cell variability compared to the open loop, and showed decreased cell-to-cell variability upon perturbation, consistent with theoretical analyses[26] (Extended Data Fig. 7).

To demonstrate the wider application potential of our integral feedback controller and its inherent capacity to confer robustness, the closed- and open-loop circuits were modified to regulate cell growth rate by exchanging *sfgfp* for *metE* (methionine synthase, Fig. 3a, b). Methionine is required for cell viability and biomass accumulation. In a host strain that lacks *metE*, cell growth can be controlled in methionine-free medium through regulation of *metE* expression[27] (Fig. 3a, b). The closed-loop growth rate is tunable with HSL in cultures grown with a fixed ARA concentration (Fig. 3c, Extended Data Fig. 8). Furthermore, when a constant environmental perturbation was applied by changing cell incubation temperature from 37 °C to 30 °C (Fig. 3d, left), the closed loop induced with 10 nM HSL and 0.2% ARA

maintained its growth rate. By contrast, the open-loop growth slowed significantly at the lower temperature (Fig. 3d, right, Extended Data Fig. 8), which suggests that the perturbation in the closed-loop strain at this set point is compensated for at 30 °C through *metE* regulation. Given that the set point is determined ratiometrically by SigW and RsiW, within the region of adaptation, any such global perturbation (for example, extrinsic noise) that affects their expression in a similar way should also be rejected by the controller.

RPA is exhibited by many endogenous biological systems[2,12,28], and understanding which network topologies allow RPA is of fundamental importance. This work is different from existing studies on this phenomenon[19–21] in two distinct ways. First, we study adaptation in the stochastic setting, in which the effects of intrinsic biochemical noise[29] are incorporated. Second, we address scenarios in which the controlled network has unknown players or interactions. We separate the 'controller network' from the 'controlled network' (see Box 1) and allow the latter to be completely arbitrary, while the former can have uncertain parameters. In this setting, our mathematical analysis proves that the integral feedback action necessary for RPA, can only be exactly implemented with biomolecular reactions by a controller that embeds the antithetic feedback-controller topology. Notably, this controller topology is known to enhance intrinsic noise and cell-to-cell heterogeneity[26,30], yet it has a universal role in ensuring RPA for the population average (or the single-cell time average) for arbitrary intracellular networks. Of note, the antithetic topology has been found in several endogenous pathways[3,31].

The rationally designed integral controller reported here represents a proof-of-concept design that establishes the feasibility of engineering robust homeostasis in synthetic biology. A suitably optimized version of this controller with expanded dynamic range should find wide applications in all scenarios in which protein expression must remain tightly regulated at the desired level, independent of other intervening processes. In metabolic engineering, for instance, robust set-point regulation of key enzymes could be used to optimize metabolic fluxes to maximize yield and minimize host toxicity. Probing endogenous pathways could also benefit from such regulation, because compensatory cellular mechanisms tend to alter expression in complex ways. A mammalian analogue of our synthetic integral feedback module could also offer exciting perspectives for cell therapy in conditions that result from dysregulation of homeostasis, by enabling the implementation of a fully autonomous and personalized intervention.

Online content
Any methods, additional references, Nature Research reporting summaries, source data, statements of data availability and associated accession codes are available at https://doi.org/10.1038/s41586-019-1321-1.

1. Yi, T.-M., Huang, Y., Simon, M. I. & Doyle, J. Robust perfect adaptation in bacterial chemotaxis through integral feedback control. *Proc. Natl Acad. Sci. USA* **97**, 4649–4653 (2000).
2. El-Samad, H., Goff, J. P. & Khammash, M. Calcium homeostasis and parturient hypocalcemia: an integral feedback perspective. *J. Theor. Biol.* **214**, 17–29 (2002).
3. Briat, C., Gupta, A. & Khammash, M. Antithetic integral feedback ensures robust perfect adaptation in noisy biomolecular networks. *Cell Syst.* **2**, 15–26 (2016).
4. Lillacci, G., Aoki, S. K., Schweingruber, D. & Khammash, M. A synthetic integral feedback controller for robust tunable regulation in bacteria. Preprint at https://www.biorxiv.org/content/10.1101/170951v1 (2017).
5. Lillacci, G., Benenson, Y. & Khammash, M. Synthetic control systems for high performance gene expression in mammalian cells. *Nucleic Acids Res.* **46**, 9855–9863 (2018).
6. Hsiao, V., de los Santos, E. L., Whitaker, W. R., Dueber, J. E. & Murray, R. M. Design and implementation of a biomolecular concentration tracker. *ACS Synth. Biol.* **4**, 150–161 (2015).
7. Ceroni, F. et al. Burden-driven feedback control of gene expression. *Nat. Methods* **15**, 387–393 (2018).
8. Huang, H.-H., Qian, Y. & Del Vecchio, D. A quasi-integral controller for adaptation of genetic modules to variable ribosome demand. *Nat. Commun.* **9**, 5415 (2018).
9. Kelly, C. L. et al. Synthetic negative feedback circuits using engineered small RNAs. *Nucleic Acids Res.* **46**, 9875–9889 (2018).
10. Åström, K. J. & Murray, R. M. *Feedback Systems: an Introduction for Scientists and Engineers* (Princeton Univ. Press, 2010).
11. Miller, P. & Wang, X.-J. Inhibitory control by an integral feedback signal in prefrontal cortex: a model of discrimination between sequential stimuli. *Proc. Natl Acad. Sci. USA* **103**, 201–206 (2006).
12. Muzzey, D., Gómez-Uribe, C. A., Mettetal, J. T. & van Oudenaarden, A. A systems-level analysis of perfect adaptation in yeast osmoregulation. *Cell* **138**, 160–171 (2009).
13. Ben-Zvi, D. & Barkai, N. Scaling of morphogen gradients by an expansion-repression integral feedback control. *Proc. Natl Acad. Sci. USA* **107**, 6924–6929 (2010).
14. Francis, B. A. & Wonham, W. M. The internal model principle of control theory. *Automatica* **12**, 457–465 (1976).
15. Sontag, E. D. Adaptation and regulation with signal detection implies internal model. *Syst. Control Lett.* **50**, 119–126 (2003).
16. Ang, J., Bagh, S., Ingalls, B. P. & McMillen, D. R. Considerations for using integral feedback control to construct a perfectly adapting synthetic gene network. *J. Theor. Biol.* **266**, 723–738 (2010).
17. Xiao, F. & Doyle, J. C. Robust perfect adaptation in biomolecular reaction networks. Preprint at https://www.biorxiv.org/content/10.1101/299057v1 (2018).
18. Briat, C., Zechner, C. & Khammash, M. Design of a synthetic integral feedback circuit: dynamic analysis and DNA implementation. *ACS Synth. Biol.* **5**, 1108–1116 (2016).
19. Ma, W., Trusina, A., El-Samad, H., Lim, W. A. & Tang, C. Defining network topologies that can achieve biochemical adaptation. *Cell* **138**, 760–773 (2009).
20. Tang, Z. F. & McMillen, D. R. Design principles for the analysis and construction of robustly homeostatic biological networks. *J. Theor. Biol.* **408**, 274–289 (2016).
21. Araujo, R. P. & Liotta, L. A. The topological requirements for robust perfect adaptation in networks of any size. *Nat. Commun.* **9**, 1757 (2018).
22. Chen, D. & Arkin, A. P. Sequestration-based bistability enables tuning of the switching boundaries and design of a latch. *Mol. Syst. Biol.* **8**, 620 (2012).
23. Helmann, J. D. *Bacillus subtilis* extracytoplasmic function (ECF) sigma factors and defense of the cell envelope. *Curr. Opin. Microbiol.* **30**, 122–132 (2016).
24. Annunziata, F. et al. An orthogonal multi-input integration system to control gene expression in *Escherichia coli*. *ACS Synth. Biol.* **6**, 1816–1824 (2017).
25. Cameron, D. E. & Collins, J. J. Tunable protein degradation in bacteria. *Nat. Biotechnol.* **32**, 1276–1281 (2014).
26. Briat, C., Gupta, A. & Khammash, M. Antithetic proportional-integral feedback for reduced variance and improved control performance of stochastic reaction networks. *J. R. Soc. Interface* **15**, 20180079 (2018).
27. Milias-Argeitis, A., Rullan, M., Aoki, S. K., Buchmann, P. & Khammash, M. Automated optogenetic feedback control for precise and robust regulation of gene expression and cell growth. *Nat. Commun.* **7**, 12546 (2016).
28. Barkai, N. & Leibler, S. Robustness in simple biochemical networks. *Nature* **387**, 913–917 (1997).
29. Elowitz, M. B., Levine, A. J., Siggia, E. D. & Swain, P. S. Stochastic gene expression in a single cell. *Science* **297**, 1183–1186 (2002).
30. Hilfinger, A., Norman, T. M., Vinnicombe, G. & Paulsson, J. Constraints on fluctuations in sparsely characterized biological systems. *Phys. Rev. Lett.* **116**, 058101 (2016).
31. Ferrell, J. E. Jr. Perfect and near-perfect adaptation in cell signaling. *Cell Syst.* **2**, 62–67 (2016).

Author contributions M.K., G.L. and S.K.A. conceived the project and designed the circuit. S.K.A., G.L. and D.S. constructed the circuits. G.L. performed the computational modelling. A.G. proved the theoretical results. S.K.A., G.L. and A.B. planned and performed the experiments and data analysis. M.K., S.K.A., A.G. and G.L. wrote the manuscript. M.K. secured funding and supervised the project.

METHODS

No statistical methods were used to predetermine sample size. The experiments were not randomized. The investigators were not blinded to allocation during experiments and outcome assessment.

Growth conditions. Cells were grown in 14-ml tubes (Greiner) in LB (1% tryptone, 0.5% yeast extract, 1% NaCl) or M9 medium supplemented with 0.2% casamino acids, 0.45% LB, 0.4% glucose, 0.001% thiamine, 0.00006% ferric citrate, 0.1 mM calcium chloride, 1 mM magnesium sulfate and 20 μg/ml uracil (Sigma-Aldrich), and incubated in an environmental shaker (Excella E24, New Brunswick) at 37 °C with shaking at 230 r.p.m. unless otherwise indicated. Antibiotics (Sigma-Aldrich) were used at the following concentrations: chloramphenicol, 34 μg/ml; spectinomycin, 100 μg/ml; ampicillin, 100 μg/ml; and kanamycin, 40 μg/ml. ARA was obtained from Sigma-Aldrich. HSL and aTc were received from Chemie Brunschwig. For all experiments, growth medium containing HSL was stored at 4 °C for the duration of the experiment and prewarmed to 37 °C 30 min before use to minimize degradation of the inducer.

Host strain and plasmids construction. Restriction enzymes, T4 DNA ligase and Taq ligase used in this study were purchased from New England Biolabs. Herculase II Fusion DNA Polymerase (Agilent) and Phusion Polymerase (New England Biolabs) were used for cloning PCR. T5 exonuclease was purchased from Epicentre. DNA isolation was performed using ZR Miniprep Classic, DNA Clean and Concentrator and Zymoclean Gel DNA Recovery Kits (Zymo Research). DNA oligonucleotide primers were synthesized by Sigma-Aldrich, Integrated DNA Technologies and Microsynth. Sequences of all plasmid and strain constructs were confirmed by Microsynth. DNA was transformed into cells as previously described[32]. All strains, plasmids, and primers used in this study are listed in Supplementary Tables 1 and 2. Plasmid maps are presented in Extended Data Figs. 9, 10. Strains and plasmids were constructed using standard cloning methods. Construction details are described in section 3 of the Supplementary Text.

Strains and plasmids used for fluorescence studies. The host strain MG1655 $\Delta araCBAD$ $\Delta lacIZYA$ $\Delta araE$ $\Delta araFGH$ $attB::lacYA177C$ $\Delta rhaSRT$ $\Delta rhaBADM$ $Tn7::tetR$, referred to as SKA703, was used for all sfGFP[33] circuits in this study.

The negative-perturbation plasmid (pSKA417, GenBank accession no. MK775703) used in these studies was constructed by placing the *M. florum* Lon protease gene M$flon$[25] under a TetR-repressible promoter (P_{TET}) on a medium-copy plasmid with a p15A origin of replication and spectinomycin resistance (Extended Data Fig. 10a.).

The closed- and open-loop plasmids used in this study were constructed modularly on a high-copy plasmid with a ColE1 origin of replication and ampicillin resistance. Initially, a closed-loop precursor plasmid (pSKA538, GenBank accession no. MK775704) was built, consisting of $P_{sigW\text{-}sRBS}$-$V5::araC::pdt3c$-$Flag::sfgfp::pdt1$, $luxR$-$P_{LUX\text{-}RBS5000}$-$sigW$, and $P_{BAD\text{-}RBS5000}$-$rsiW$. (Extended Data Fig. 10b). An open-loop variant precursor plasmid (pSKA539, GenBank accession no. MK775705) was also constructed with feedback disabled by removing the $P_{BAD\text{-}RBS5000}$-$rsiW$ module (Extended Data Fig. 10b). The final versions of the circuits used in this study (pSKA562 and pSKA563, GenBank accession no. MK775706 and MK775707) were constructed by adding a second tandem copy of $P_{sigW\text{-}sRBS}$-$V5::araC::pdt3c$-$Flag::sfgfp::pdt1$ to each plasmid (Extended Data Fig. 10c).

Strains and plasmids used for growth-rate control studies. A variant of SKA703 (SKA1328) with deleted endogenous $metE$ was used for all growth-rate control experiments.

Closed-loop growth-rate control plasmid pSKA570 (GenBank accession no. MK775708) and open-loop growth-rate control plasmid pSKA571 (GenBank accession no. MK775709) were constructed by exchanging $sfgfp$ for $metE$ with a weak ribosomal-binding site (Extended Data Fig. 10d). Open-loop variant pSKA571-p15A (GenBank accession no. MK775710) is identical to pSKA571 but with a lower-copy p15A origin of replication (Extended Data Fig. 10d).

V5-AraC-Pdt#3c immunoblot. During the course of this study it was observed that the efficiency of MfLon protease-dependent degradation was not only affected by the degradation tag sequence but also by the tagged protein itself. Originally, a Pdt#1 degradation tag was used for both AraC and sfGFP. However, immunoblot analysis of V5-AraC-Pdt#1 suggested that AraC was being more efficiently degraded by the MfLon protease than sfGFP (data not shown). Changing the AraC degradation tag from Pdt#1 to the weaker Pdt#3c tag resulted in an improvement in matching sfGFP degradation rates (Extended Data Fig. 5).

SKA703 pSKA417 pSKA539 (open-loop, $V5::araC::pdt3c$, $Flag::sfgfp::pdt1$) was grown overnight in 5 ml M9–0.2% ARA and appropriate antibiotics. SKA703 (no-plasmid negative-control strain) was grown overnight in 5 ml M9–0.2% ARA (antibiotic-free). The overnight cultures were diluted into 5-ml aliquots of M9–0.2% ARA and appropriate antibiotics containing 5 nM HSL with or without 10 ng/ml aTc at a low optical density (OD, 0.00008 starting OD for SKA703 pSKA417 pSKA539; 0.00004 starting OD for negative-control SKA703), and incubated for 4.5 h before being rediluted into 5-ml aliquots of prewarmed matching

medium at low OD (SKA703 pSKA417 pSKA539 at 0.00004 OD; SKA703 at 0.00001 OD) followed by another 4.5 h of incubation.

After 9 h of induction, culture samples were measured in triplicate for sfGFP fluorescence by flow cytometry. Aliquots (4.5 ml) of each culture were pelleted at 4 °C. Cell pellets were resuspended in 1× lysis buffer (1× BugBuster (Merck and Cie), 1× cOmplete EDTA-free Protease Inhibitor (Roche Diagnostics), 60 mM Tris-HCl pH 6.8 (Sigma-Aldrich Chemie), 10% glycerol (Axon Laboratory), 2% SDS (Sigma-Aldrich Chemie), 5% β-mercaptoethanol (Sigma-Aldrich Chemie), 1 mM phenylmethylsulfonyl fluoride (Sigma-Aldrich Chemie). Lysis buffer volume was calculated as OD × 4,500 μl/5 for all cultures. Cells were lysed at 95 °C for 10 min and used immediately after preparation.

Freshly prepared 10-μl aliquots of lysates and 0.75 μl Odyssey Protein Marker (Li-Cor GmbH) were run on a NuPAGE 4–12% Bis-Tris mini gel (1 mm, 15 well, Invitrogen) with NuPAGE MES SDS Running Buffer (Invitrogen) at 200 V for 40 min under denaturing conditions.

Proteins were transferred to Immobilon-FL PVDF membrane (Merck and Cie) using NuPAGE Tris-glycine-10% methanol transfer buffer (Invitrogen) at 30 V for 1 h (XCell II Blot Module, Invitrogen). The membrane was dried overnight post-transfer.

The dried membrane was reactivated in methanol before being washed with water and stained for total protein using REVERT Total Protein Stain (Li-Cor) as recommended by the manufacturer. The stained membrane was imaged immediately in the 700 nm channel with a Li-Cor Odyssey CLx equipped with Image Studio v.2.1.10 software (169-μm resolution, medium quality, auto intensity).

After imaging, the membrane was rinsed with water and then blocked for 1 h at room temperature in Li-Cor Odyssey Blocking Buffer(PBS). The membrane was incubated with 1:5,000 mouse V5 antibody (E10) (AB53418, Abcam) in blocking buffer with 0.1% Tween-20 (Sigma-Aldrich Chemie) at room temperature for one hour before being washed five times with phosphate-buffered saline (PBS) containing 0.1% Tween-20, 5 min each wash, followed by 1 h room-temperature secondary antibody incubation (1:10,000 Li-Cor goat α-mouse IRDye800CW 925-32210) in blocking buffer with 0.1% Tween-20. The membrane was washed 5 times with PBS containing 0.1% Tween-20, twice with PBS (no Tween-20), and scanned on a Li-Cor Odyssey CLx (700-nm and 800-nm channels, 169-μm resolution, medium quality, auto intensity).

Densitometry analysis of the total protein and V5 band intensities were analysed using Li-Cor Image Studio v.2.1.10 software. Background subtraction was performed using median pixel values and a border width of three. All lanes were within the linear detection range of both the REVERT Total Protein Stain and V5 antibody staining with the exception of the SKA703 negative control, which was below the linear detection range for V5 signal (data not shown). The V5 immunoblot signal was normalized to the total detected protein for each lane.

High throughput ARA and HSL titrations. All titration assays to measure the response of closed-loop circuit strain SKA703 pSKA417 pSKA562 to different inducer concentrations were performed on a Tecan EVO 200 robotic platform in 96-well plates (Nunc). For each biological replicate, an independent master culture was grown at 37 °C with shaking for a minimum of 12 h to stationary phase in M9 medium with 0.2% ARA and antibiotics. The final volume of each well was 150 μl. To start the experiment, the master culture was diluted 1:10,000 in individual wells at 4 °C containing M9 minimal medium with antibiotics and the desired combinations of inducers (HSL and ARA). Each biological replicate was cultured in medium prepared independently from the other replicates. This first dilution was incubated at 37 °C for 6 h, and then diluted again 1:10,000 in a fresh plate at 4 °C, with each well being diluted into the corresponding well of the new plate (to maintain the same inducer concentrations). The second dilution was incubated at 37 °C for 5 h, after which the plate was analysed at room temperature with flow cytometry. The reported data are from four independent biological replicates pooled from experiments performed on two separate days.

Step responses. Five-millilitre aliquots of M9 medium with appropriate antibiotics and 0.15% or 0.2% ARA were inoculated with SKA703 pSKA417 pSKA562 (closed loop) from glycerol freeze stocks at an OD of 8×10^{-8}. The cultures were incubated for 9 h overnight at 37 °C with shaking. In the morning, the overnight cultures were in early logarithmic phase. The overnight cultures were diluted into 5 ml fresh prewarmed induction medium at 0.005 OD and incubated at 37 °C with shaking. The 0.15% overnight ARA cultures were diluted into medium containing 0.15% ARA and 5 nM HSL. The 0.2% overnight ARA cultures were diluted into medium containing 0.2% ARA and either 5.5 nM, 7.5 nM or 8.5 nM HSL. Every 1.5 h, ODs were measured and all cultures were rediluted into matching prewarmed induction medium at 0.005 OD. At every dilution point, three 200-μl samples of culture were collected and measured by flow cytometry and the average of the technical replicates were used. ODs were used to calculate cell growth rate. The reported data are from three independent biological replicates pooled from experiments performed on the same day. For each biological replicate, a separate

stock of medium was independently prepared and used only for that particular replicate. Every biological replicate was started from its own independently prepared overnight culture.

Induction of negative perturbation. SKA703 pSKA417 pSKA562 (closed loop) and SKA703 pSKA417 pSKA563 (open loop) strains were grown overnight in M9 medium containing 0.1%, 0.15%, and 0.2% ARA. Overnight cultures were diluted into fresh medium with matching ARA concentrations and different concentrations of HSL (3.5 and 4 nM HSL with 0.1% ARA, 5, 5.5, and 7 nM HSL with 0.15% ARA, 5.5, 7, and 9 nM HSL with 0.2% ARA) with or without 10 ng/ml aTc at 0.00004 OD and incubated at 37 °C with shaking. Additionally, the open loop was also induced with 0.2% ARA and 0 nM HSL to match the unperturbed output fluorescence of the closed loop in 0.2% ARA and 7 nM HSL. At 4.5 h, each culture was diluted into fresh matching prewarmed induction medium with the same inducers at 0.00002 OD. At 9 h, 3 200-μl aliquots of culture were collected and measured by flow cytometry and the average of the technical replicates was used. The OD of the cultures were read at time 0, 4.5 and 9 h and used to estimate the growth rate for each culture. The reported data are from three independent biological replicates pooled from experiments performed on two separate days. For each biological replicate, a separate stock of medium was independently prepared and used only for that particular replicate. Every biological replicate was started from its own independently prepared overnight culture.

Dynamic negative perturbation. Five-millilitre aliquots of M9 medium with appropriate antibiotics and 0.2% ARA were inoculated with SKA703 pSKA417 pSKA562 (closed loop) and SKA703 pSKA417 pSKA563 (open loop) from glycerol freeze stocks at an OD of 8×10^{-8}. The cultures were incubated for 9 h overnight at 37 °C with shaking. In the morning, the overnight cultures were in early logarithmic phase. The overnight cultures were diluted in 5 ml fresh prewarmed induction medium at 0.005 OD and incubated at 37 °C with shaking. The overnight cultures were diluted into medium containing 0.2% ARA and 5.5 nM HSL. Every 1.5 h, all cultures were rediluted into matching prewarmed induction medium. At 4.5 h, cells were at or close to steady state (time 0 h in Fig. 2f). After 6 h of incubation (time 1.5 h in Fig. 2f), each culture was diluted into two separate aliquots of medium and 10 ng/ml aTc was added to one aliquot and subsequent dilutions with these aTc-induced cultures were made with aTc-containing medium. At every dilution point, 3 200-μl samples of culture were collected and measured by flow cytometry and the average of the technical replicates were used. The reported data are from three independent biological replicates pooled from experiments performed on two separate days. For each biological replicate, a separate stock of medium was independently prepared and used only for that particular replicate. Every biological replicate was started from its own independently prepared overnight culture.

Growth-rate control. *Growth-rate titration.* SKA1328 pSKA570 was grown overnight in M9 medium supplemented with 0.2% ARA. Overnight culture was diluted 1:5,000 into 5-ml aliquots of methionine-dropout medium (M9 salts, 0.4% glucose, 0.001% thiamine, 20 μg/ml uracil, 0.00006% ferric citrate, 0.1 mM calcium chloride, 1 mM magnesium sulfate, and 19 amino acids at 40 μg/ml, methionine-free) containing 80 ng/ml methionine, 0.2% ARA, and 10, 20, 30, or 40 nM HSL. Cultures were incubated at 37 °C with shaking for 12 h. Cultures were then diluted into fresh 5-ml aliquots of prewarmed dropout medium with matching inducer concentrations at an OD of 0.0005. Immediately after dilution, 75-μl samples were removed and mixed with 79 μl of 500 μg/ml rifampicin (Sigma-Aldrich Chemie) in phosphate-buffered saline and 21 μl of 2-μm AccuCount Blank Particles (Spherotech) in a 96-well plate (Greiner) on ice. Samples were collected every hour for 9 h. Absolute cell counts were determined by flow cytometry and used to calculate the actual cell concentration over time. An example of the gating strategy is presented in Extended Data Fig. 8d. Steady-state growth rate was calculated by taking the logarithm of the absolute cell counts and performing linear regression using a time point interval in which cells showed stable linear behaviour (intervals indicated in the source data). The reported data are from three independent biological replicates pooled from experiments performed on the same day. For each biological replicate, a separate stock of medium was independently prepared and used only for that particular replicate. Every biological replicate was started from its own independently prepared overnight culture.

Robustness of growth-rate control to different temperatures. SKA1328 pSKA570 (closed-loop) and SKA1328 pSKA571 (open-loop) were grown overnight in M9 medium with 0.2% ARA and appropriate antibiotics. Overnight cultures were diluted 1:5,000 into 5 ml aliquots of methionine-dropout medium (as described for growth-rate titrations) containing 80 ng/ml methionine, 0.2% ARA, 10 nM HSL, and appropriate antibiotics. Cultures were incubated at 37 °C or 30 °C with shaking for 12 h to ensure that induced cells were in a state of active growth and that any residual methionine in the medium was fully metabolized. Cultures were then diluted into fresh 5-ml aliquots of prewarmed dropout

medium (methionine-free) with matching inducer concentrations and antibiotics at an OD of 0.0005 for 37 °C cultures or 0.001 for 30 °C cultures. The 37 °C cultures were started at a lower OD than the 30 °C cultures to be able to follow the 37 °C cultures over the duration of the experiment without the cells growing out of early exponential phase. Immediately after dilution, 75-μl samples were removed and mixed with 79 μl of 500 μg/ml rifampicin (Sigma-Aldrich Chemie) in phosphate-buffered saline and 21 μl of 2-μm AccuCount Blank Particles (Spherotech) in a 96-well plate (Greiner) on ice. Samples were collected every hour for 12 h. Absolute cell counts were determined by flow cytometry and used to calculate the actual cell concentration over time. An example of the gating strategy is presented in Extended Data Fig. 8d. Steady-state growth rate was calculated by taking the logarithm of the absolute cell counts and performing linear regression as described above for growth-rate titrations. The reported data are from three independent biological replicates pooled from experiments performed on two separate days. For each biological replicate, a separate stock of medium was independently prepared and used only for that particular replicate. Every biological replicate was started from its own independently prepared overnight culture.

In an effort to match the growth rate of the closed-loop at 37 °C, SKA1328 containing reduced plasmid-copy-number open-loop circuit pSKA571-p15A was used. To minimize the growth rate of the open loop, it was decided not to induce the open loop with HSL as the leaky expression of *metE* was sufficient. Growth-rate control experiments were performed with 0.2% ARA and 0 nM HSL. Dilutions, sampling, and growth-rate calculations were performed as described above for growth-rate titrations. The reported data are from three independent biological replicates pooled from experiments performed on two separate days. For each biological replicate, a separate stock of medium was independently prepared and used only for that particular replicate. Every biological replicate was started from its own independently prepared overnight culture.

As a reference for the closed- and open-loop growth-rate control circuits, endogenous *metE+* wild-type strain SKA703 with empty plasmid vector pSKA47 was also tested as described above with modifications to account for faster growth. The strain was grown overnight in M9 medium with 0.2% ARA and appropriate antibiotics. Overnight cultures were diluted 1:100,000 or 1:50,000 into 5 ml aliquots of methionine-dropout medium (as described for growth-rate titrations) containing 80 ng/ml methionine, 0.2% ARA, 10 nM HSL, and appropriate antibiotics. The 1:100,000 dilutions were incubated at 37 °C and the 1:50,000 dilutions were incubated at 30 °C with shaking for twelve hours. Cultures were then diluted into fresh 5-ml aliquots of prewarmed dropout medium (methionine-free) with matching inducer concentrations and antibiotics at an OD of 0.0001 for 37 °C cultures or 0.0002 for 30 °C cultures. Cultures were sampled as described above every 30 min for up to 8 h. Cultures at 37 °C were terminated at 6.5 h as they grew out of early exponential phase. Growth-rate calculations were performed as described above for growth-rate titrations. The reported data are three independent biological replicates pooled from experiments performed on two separate days. For each biological replicate, a separate stock of medium was independently prepared and used only for that particular replicate. Every biological replicate was started from its own independently prepared overnight culture.

Flow cytometry. The samples from the high throughput titrations in 96-well plates were analysed on a LSRII Fortessa flow cytometer (BD Biosciences) equipped with the FACSDiva v.8.0.1 software program and a high throughput sampler. sfGFP was measured with a 488-nm laser and 530/30 and 505 low-pass emission filters; the voltage gains of the instrument were set as follows: forward scatter 500 V, side scatter 300 V, sfGFP 900 V. A minimum of 5,000 events were collected for each well using thresholds of 500 FSC-H and 500 SSC-H.

Fluorescence measurements for the immunoblot lysate preparation cultures, step responses, steady-state negative perturbation, dynamic perturbation, and absolute cell count measurements for the growth-rate control experiments were performed using a CytoFlex S flow cytometer (Beckman Coulter) equipped with CytExpert v.2.1.092 software. sfGFP was measured with a 488-nm laser and 525/40 bandpass filter; the gain settings of the instrument were as follows: forward scatter 100, side scatter 100, sfGFP 500. Thresholds of 2,500 FSC-H and 1,000 SSC-H were used for all samples. Fifty thousand events were collected for the lysate preparation, step response experiments, steady-state disturbance rejection experiments, and dynamic perturbation experiments and 1,000 AccuCount Blank Particles were collected for the growth-rate control experiments.

The raw flow cytometry data were gated with FlowJo v.10 (Treestar) (Extended Data Figs. 3a, 8d) and cell autofluorescence was subtracted from sfGFP measurements. The data were then further processed using custom R v.3.5.0 scripts or plotted with GraphPad Prism 7. Background fluorescence is plotted in Extended Data Fig. 3b. Excel was used to perform *t*-tests (unpaired, two-tailed, unequal variance).

Reporting summary. Further information on research design is available in the Nature Research Reporting Summary linked to this paper.
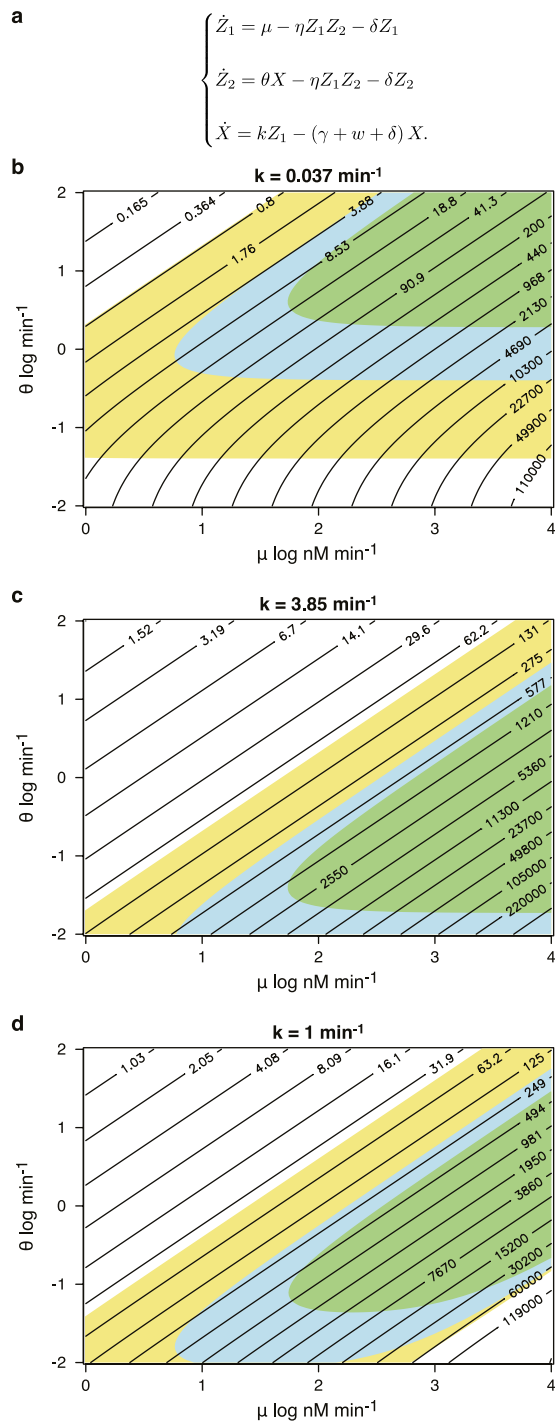
Data availability

All relevant data are included as Source Data and/or are available from the corresponding author on reasonable request. Plasmid sequences are deposited in GenBank under the accession codes MK775703–MK775710. Strains and plasmids used in this study are available from the corresponding author on reasonable request.

Code availability

Code used for simulations is available on reasonable request from the corresponding author.

32. Chung, C. T., Niemela, S. L. & Miller, R. H. One-step preparation of competent *Escherichia coli*: transformation and storage of bacterial cells in the same solution. *Proc. Natl Acad. Sci. USA* **86**, 2172–2175 (1989).
33. Pédelacq, J.-D., Cabantous, S., Tran, T., Terwilliger, T. C. & Waldo, G. S. Engineering and characterization of a superfolder green fluorescent protein. *Nat. Biotechnol.* **24**, 79–88 (2006).

a

$$\begin{cases} \dot{Z}_1 = \mu - \eta Z_1 Z_2 - \delta Z_1 \\ \dot{Z}_2 = \theta X - \eta Z_1 Z_2 - \delta Z_2 \\ \dot{X} = kZ_1 - (\gamma + w + \delta)\, X. \end{cases}$$

b $k = 0.037$ min^{-1}

c $k = 3.85$ min^{-1}

d $k = 1$ min^{-1}

Extended Data Fig. 1 | Deterministic modelling of the non-ideal antithetic integral feedback circuit. a, Deterministic model of the non-ideal antithetic integral feedback (AIF) circuit. **b, c**, Output steady state and steady-state error for the non-ideal AIF circuit with dilution and negative disturbance. The black lines indicate curves of constant output steady state (in nM) for a dilution rate corresponding to a typical bacterial growth rate. The green, blue and yellow shadings denote the regions of the parameter space in which the relative output steady-state error is less than 5% for dilution rates corresponding to typical values for bacteria, yeast and mammalian cells, respectively. $k = 0.037$ min^{-1} in **b** and 3.85 min^{-1} in **c**. **d**, Output steady state and steady-state error for the non-ideal AIF circuit with dilution, negative disturbance and actuator saturation. The black lines indicate curves of constant output steady state for a dilution rate corresponding to a typical bacterial growth rate. The green, blue and yellow shadings denote the regions of the parameter space in which the relative output steady-state error is less than 5% for dilution rates corresponding to typical values for bacteria, yeast and mammalian cells, respectively. In this plot $k = 1$ min^{-1}.
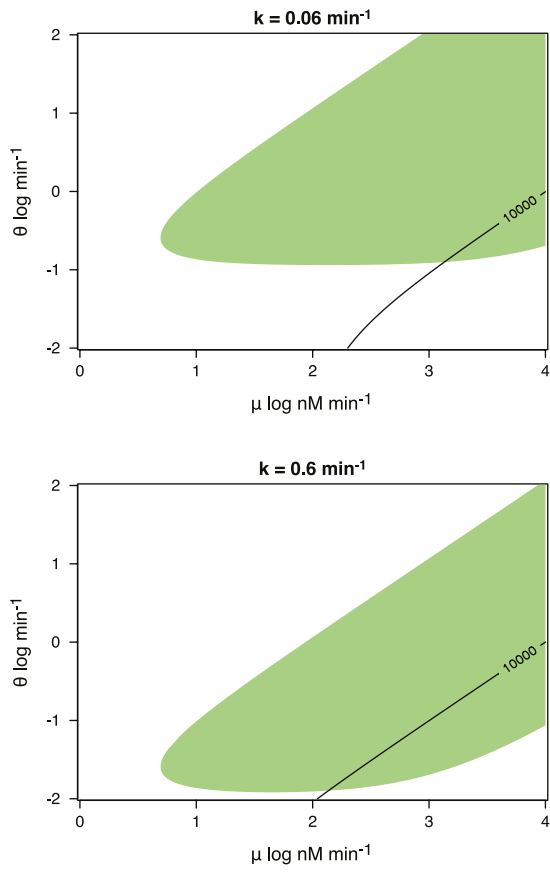
Extended Data Fig. 2 | Dependency of the adaptation region of the non-ideal AIF circuit with dilution, negative disturbance and saturation on the actuator gain k. The black curve has constant steady-state of 10,000 nM for a dilution rate corresponding to a typical bacterial growth rate. The green shading shows the region of the parameter space in which the relative output steady-state error is less than 5%.
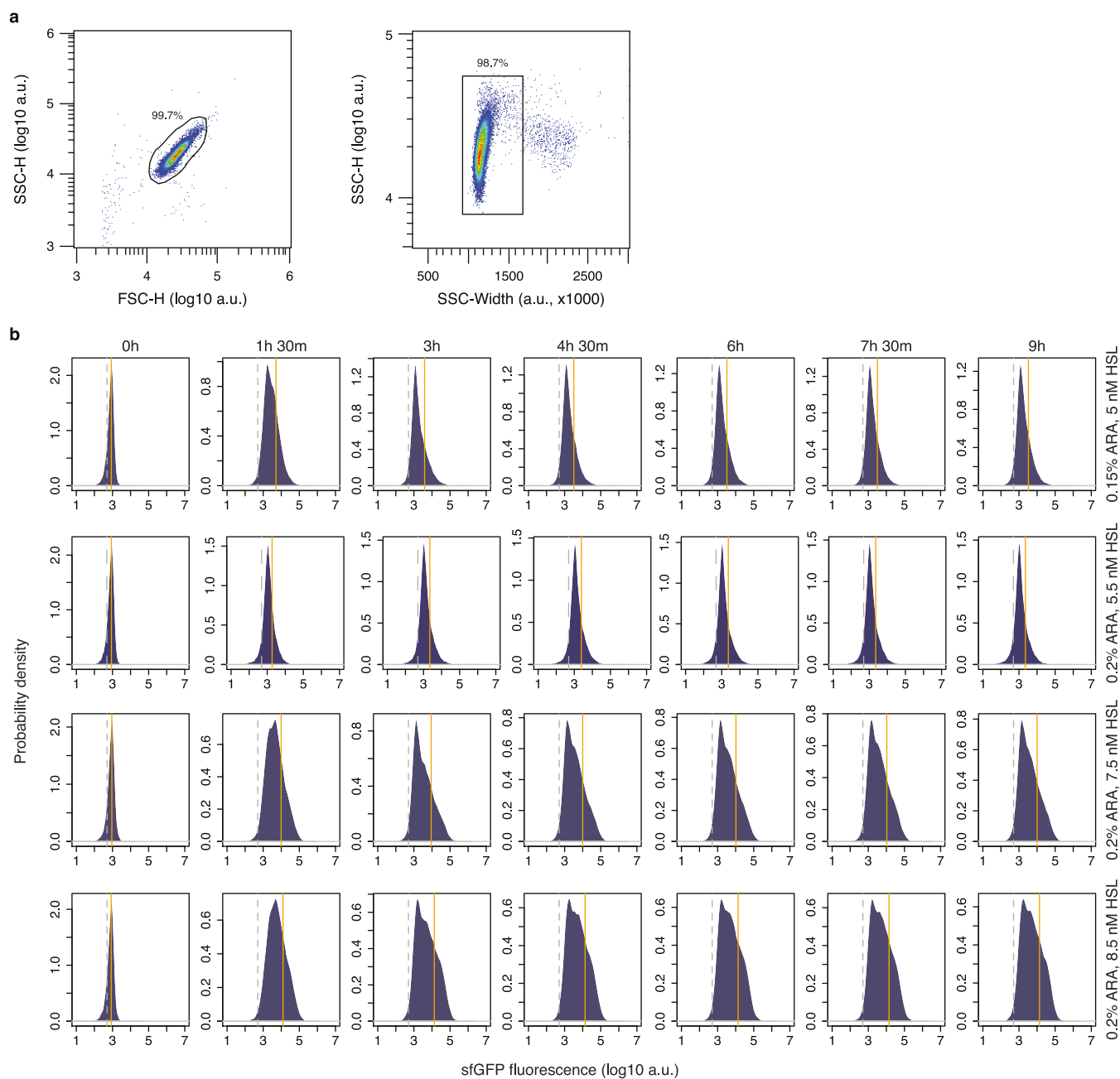
Extended Data Fig. 3 | Fluorescence distributions of dynamic closed-loop circuit response. a, Example of gating strategy for flow cytometry fluorescence measurements. Cells are first gated manually from background noise using a FSC-H–SSC-H plot (left). The gated cells are then selected for singlets using a SSC-width–SSC-H plot (right). The percentage of events within each gate is indicated. **b**, sfGFP fluorescence distributions for the dynamic step-response experiment in Fig. 2d as a function of time. The vertical orange line represents the mean. The vertical dashed grey line represents the mean of the background distribution, which was obtained by measuring non-fluorescent SKA703 cells containing pSKA570 and pSKA417. Data are representative of three biological replicates.
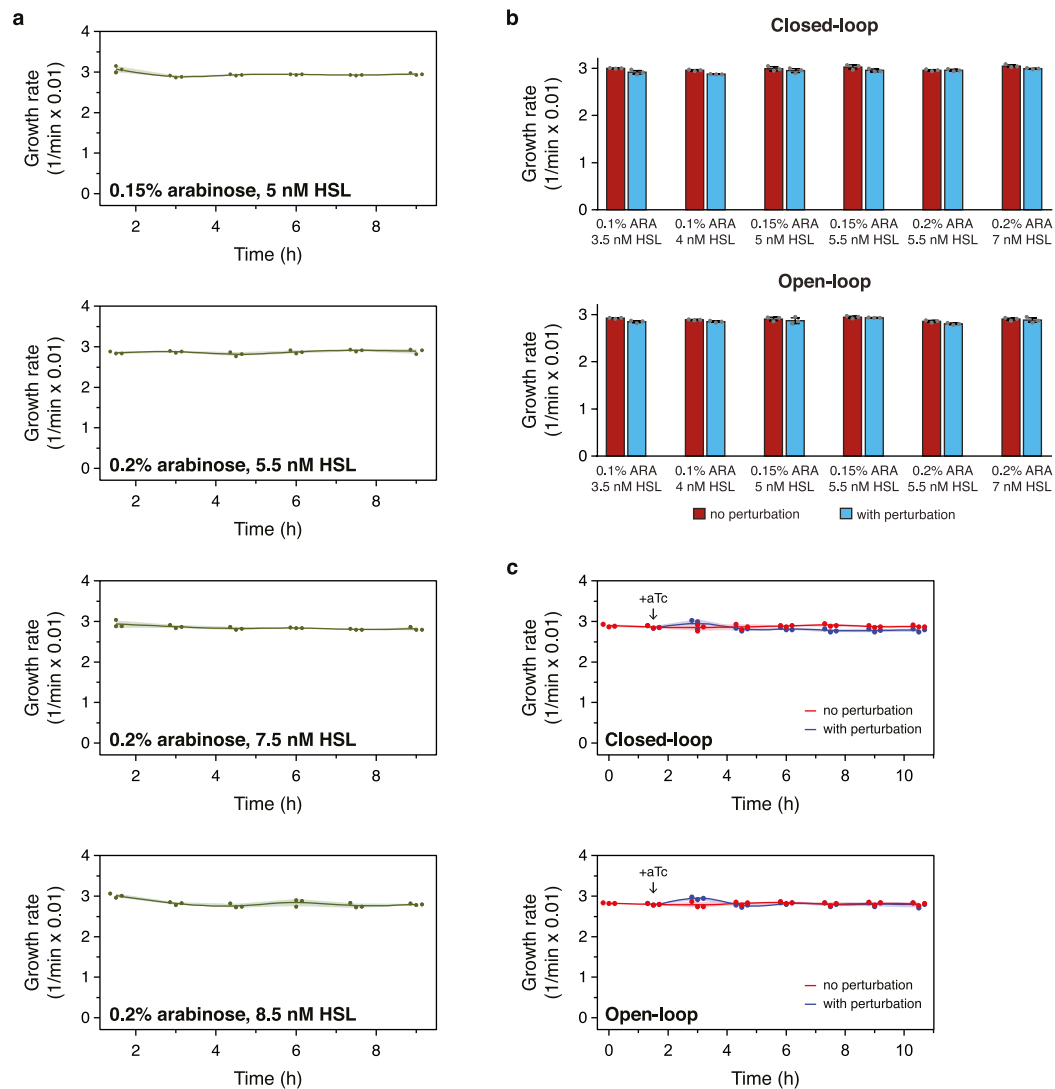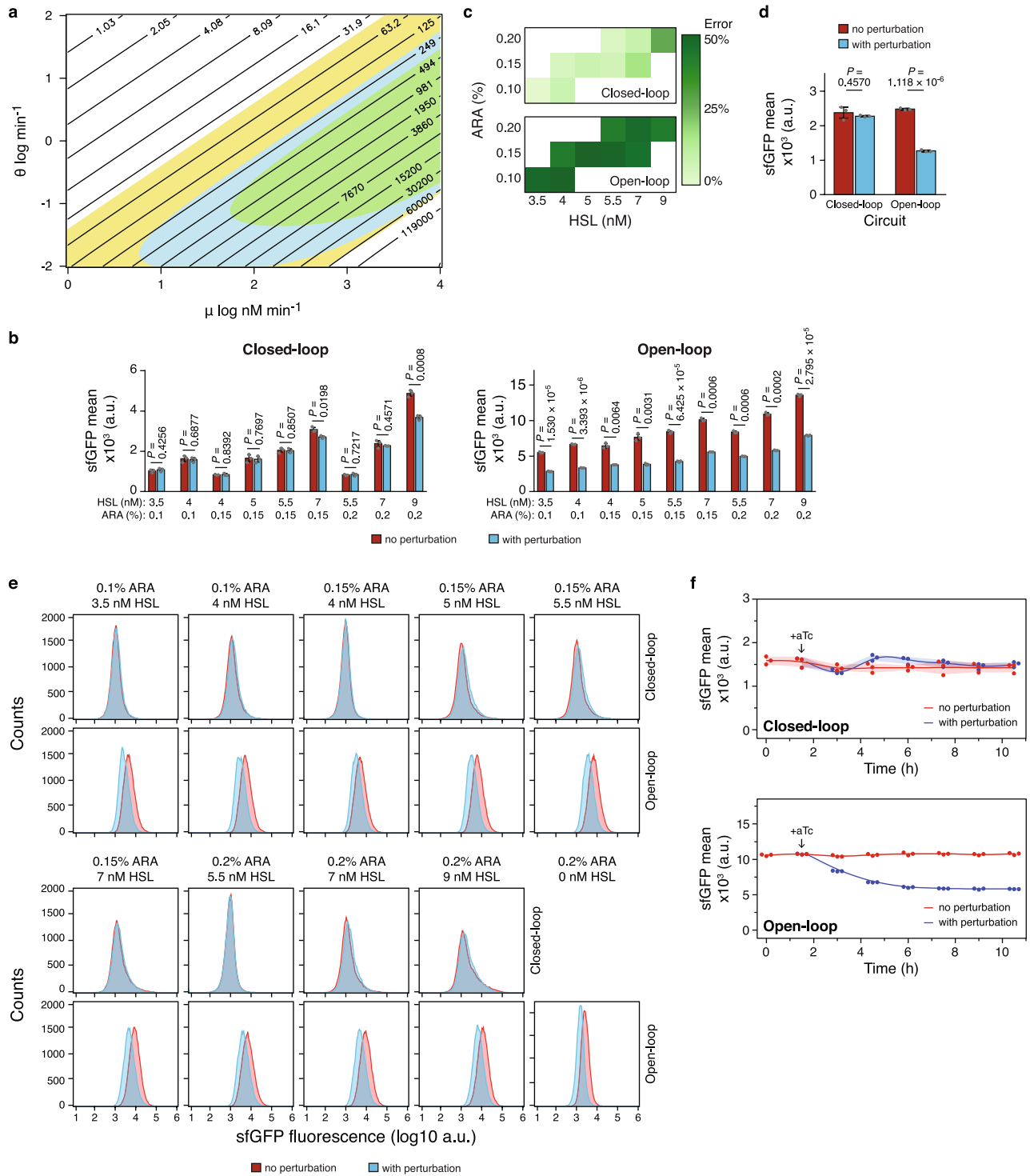
Extended Data Fig. 4 | AIF circuit with sfGFP output does not affect cell growth rate. a, Dynamic growth rates for closed-loop step responses presented in Fig. 2d. Circles indicate the independent biological replicates ($n = 3$) and the average of the points is fit with a cubic spline. Shaded regions indicate the s.d. **b**, Steady-state growth rates for closed- and open-loop circuits in Fig. 2e. Data show mean ± s.d. ($n = 3$). Circles indicate the independent biological replicates. **c**, Dynamic growth rates for closed- and open-loop circuits in Fig. 2f. Circles indicate the independent biological replicates ($n = 3$) and the average of the points is fit with a cubic spline. Shaded regions indicate the s.d.
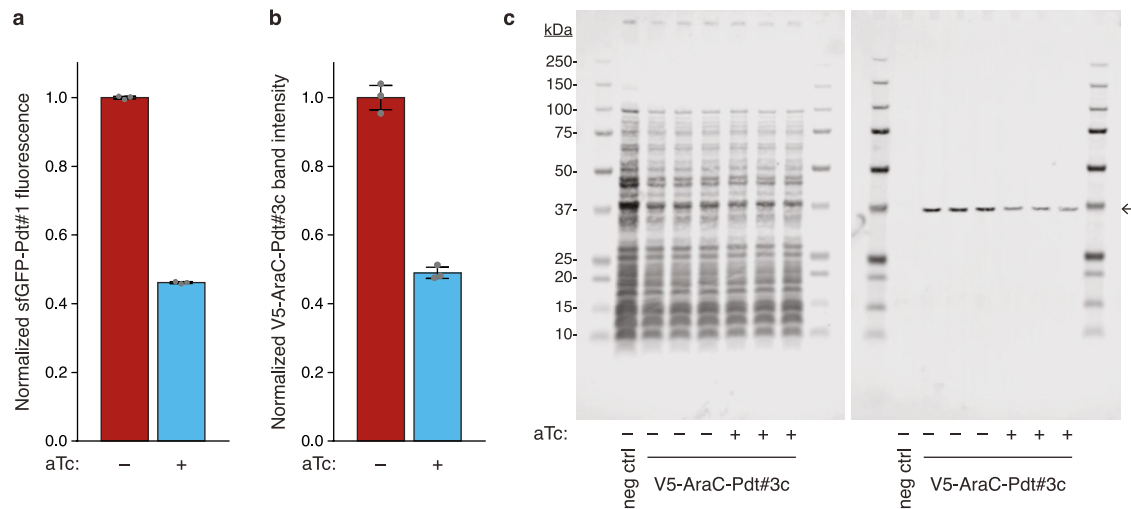
Extended Data Fig. 5 | *Mf*Lon protease-mediated degradation of AraC and sfGFP is closely matched. Protein levels of V5-tagged AraC with a Pdt#3c degradation tag with and without aTc-induction of M*flon* were compared to fluorescence levels of sfGFP with a Pdt#1 tag. **a**, Mean sfGFP fluorescence of the cultures used for lysate preparation. sfGFP fluorescence normalized to the predisturbance level. Error bars denote standard deviation (*n* = 3). Circles denote the individual replicates. **b**, Means of V5-tagged AraC immunoblot band intensities normalized to total protein. Band intensity normalized to the pre-disturbance level. Error bars denote standard deviation (*n* = 3). Circles denote the individual replicates. **c**, Immunoblot. Left, total protein on membrane post-transfer. Right, V5-AraC-Pdt#3c immunoblot. V5-AraC-Pdt#3c is indicated with an arrow. SKA703 was included as a no-plasmid negative control (neg ctrl). For immunoblot source data, see Supplementary Fig. 1. Data are representative of three independent experiments.

Extended Data Fig. 6 | Output steady-state error of the AIF circuit.
a, Steady-state error simulations of the non-ideal AIF circuit with dilution, negative disturbance and actuator saturation from Extended Data Fig. 1d. The black lines indicate curves of constant output steady state (in nM) for a dilution rate corresponding to a typical bacterial growth rate. The green, blue and yellow shading denotes the regions of the parameter space in which the relative output steady-state error is less than 5% for dilution rates corresponding to bacteria, yeast and mammalian cells, respectively. In this plot $k = 1$ min^{-1}. **b**, Non-normalized output steady states of closed- and open-loop circuits in vivo in the presence of *Mf*Lon protease perturbation from Fig. 2e and four additional HSL and ARA conditions. Data show mean ± s.d. for $n = 3$ independent biological replicates (grey circles). Two-tailed, unpaired, unequal variance *t*-test. **c**, Heat map of the steady-state error for the closed-loop and open-loop data presented in **b**. **d**, Matched output steady states of the closed-loop circuit with 0.2% ARA and 7 nM HSL and the open-loop circuit with 0.2% ARA and 0 nM HSL. Data show mean ± s.d. for $n = 3$ independent biological replicates (grey circles). Two-tailed, unpaired, unequal variance *t*-test. **e**, Fluorescence distributions for the closed- and open-loop circuits in **b**. Data are representative of three independent experiments. **f**, Non-normalized output for the closed- and open-loop dynamic disturbance rejection experiment presented in Fig. 2f. Mean sfGFP is plotted as a function of time and fit with a cubic spline for $n = 3$ independent biological replicates. Shaded regions indicate the s.d.
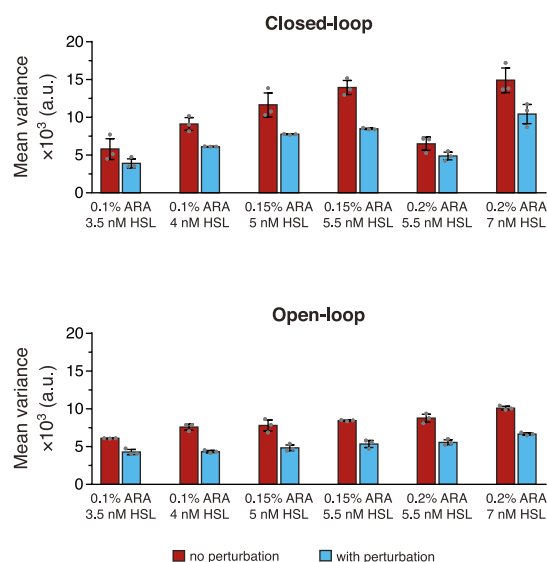
Extended Data Fig. 7 | Application of a negative perturbation reduces the output variance of closed-loop and open-loop circuits. sfGFP fluorescence variance for the closed-loop and open-loop circuits in Fig. 2e. Data show mean ± s.d. for $n = 3$ independent biological replicates (grey circles).
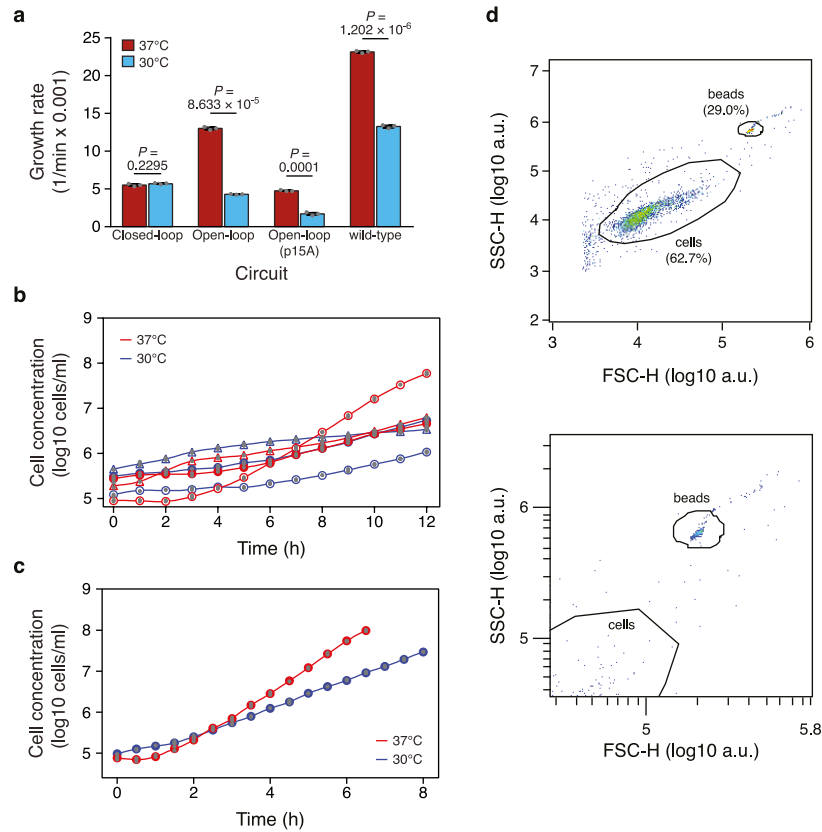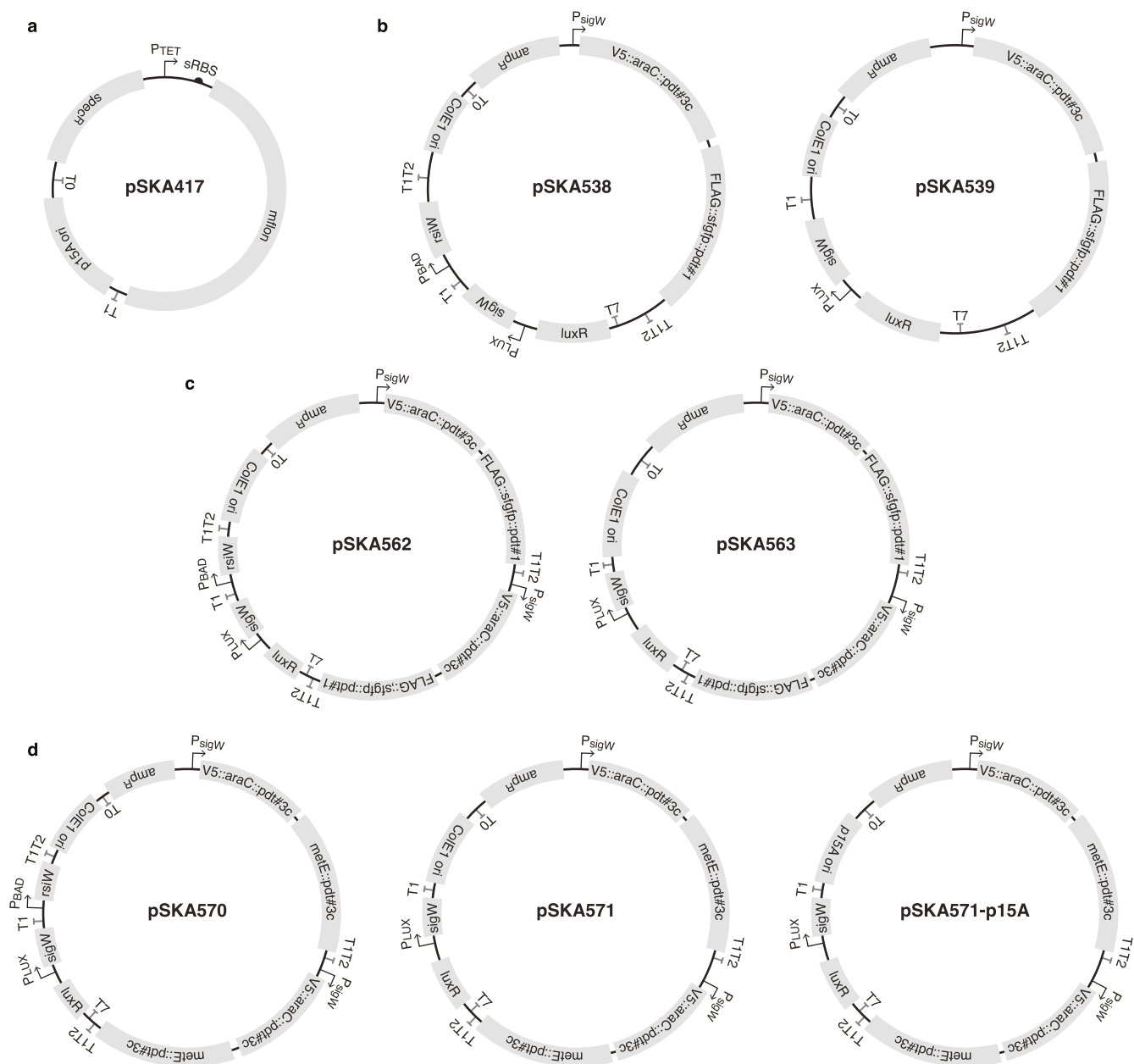
Extended Data Fig. 8 | Additional growth-rate control data. a, Non-normalized growth-rate data for the closed- and open-loop growth-rate control circuits in Fig. 3d induced with 0.2% ARA and 10 nM HSL, an open-loop growth-rate control circuit with reduced-plasmid-copy number (pSKA571-p15A, open loop (p15A)) induced with 0.2% ARA and 0 nM HSL, and a *metE+* wild-type strain (SKA703, wild type) containing an empty plasmid vector induced with 0.2% ARA and 10 nM HSL. Closed- and open-loop circuits were placed in a Δ*metE* host strain for testing. All strains were grown in methionine-free medium at 37 °C and 30 °C and steady-state growth rates were determined. Data show mean ± s.d. for $n = 3$ independent biological replicates (grey circles). Two-tailed, unpaired, unequal variance *t*-test. **b**, Cell concentration plotted over time for the closed-loop circuit (closed circles), the open-loop circuit (open circles) and the reduced-plasmid-copy open-loop circuit (pSKA571-p15A, open triangles) in **a** and Fig. 3d. Grey circles indicate the independent biological replicates ($n = 3$) and the average of the points is fit with a cubic spline. Error bars indicate the s.d. **c**, Cell concentration plotted over time for the wild-type strain from **a**. Grey circles indicate $n = 3$ independent biological replicates and the average of the points is fit with a cubic spline. Error bars indicate the s.d. **d**, Example of gating strategy for absolute cell counts. Cells and beads are gated manually from background noise using a FSC-H/SSC-H plot (top). The bead population can be seen in a magnified view (bottom). The percentage of events within each gate is indicated.
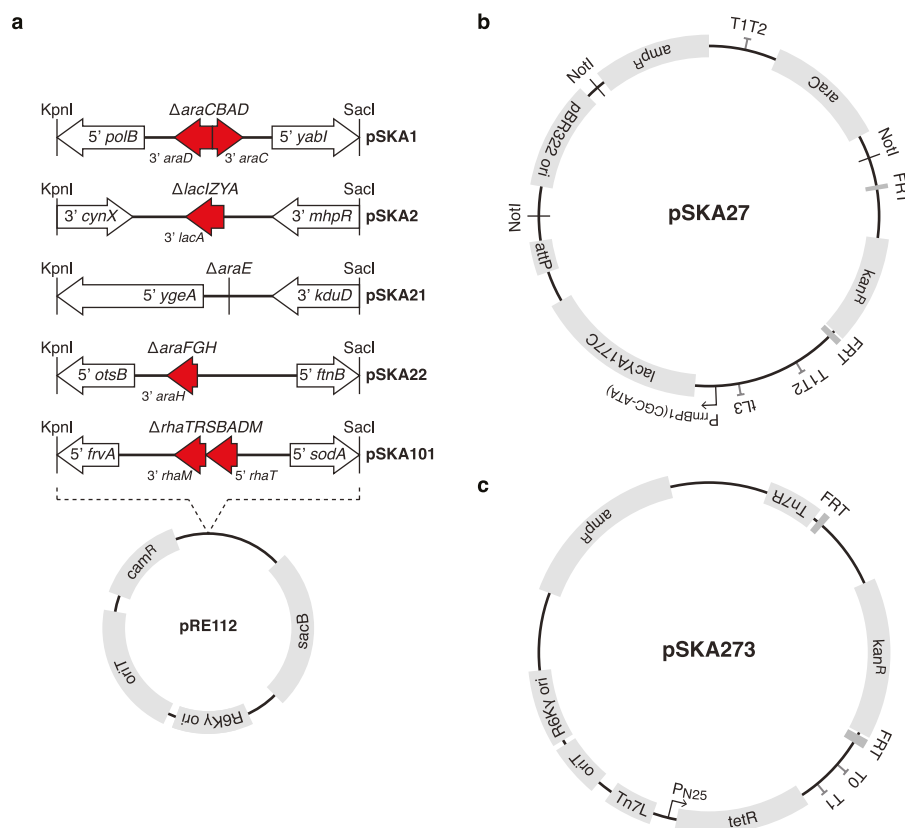
Extended Data Fig. 9 | Plasmids used in this study to construct host strain SKA703. a, Suicide plasmids used to delete the ARA, lactose and rhamnose metabolic pathways from MG1655. The disrupted gene region and flanking upstream and downstream genomic sequences were inserted into suicide vector pRE112. The remaining deletion scar is indicated in red. **b**, λ-Integration plasmid used for the chromosomal integration of constitutively expressed *lacYA177C*. **c**, *Tn7*-integration plasmid used for the chromosomal integration of constitutively expressed *tetR*.

Extended Data Fig. 10 | Circuit plasmids used in this study. a, M*flon* perturbation plasmid. **b**, Synthetic-circuit precursor plasmids. **c**, Closed- and open-loop plasmids. **d**, Closed- and open-loop growth-rate control plasmids.

nature research

Corresponding author(s):	Mustafa Khammash
Last updated by author(s):	Apr 11, 2019

Reporting Summary

Nature Research wishes to improve the reproducibility of the work that we publish. This form provides structure for consistency and transparency in reporting. For further information on Nature Research policies, see Authors & Referees and the Editorial Policy Checklist.

Statistics

For all statistical analyses, confirm that the following items are present in the figure legend, table legend, main text, or Methods section.

n/a	Confirmed	
☐	☒	The exact sample size (n) for each experimental group/condition, given as a discrete number and unit of measurement
☐	☒	A statement on whether measurements were taken from distinct samples or whether the same sample was measured repeatedly
☐	☒	The statistical test(s) used AND whether they are one- or two-sided *Only common tests should be described solely by name; describe more complex techniques in the Methods section.*
☐	☒	A description of all covariates tested
☐	☒	A description of any assumptions or corrections, such as tests of normality and adjustment for multiple comparisons
☐	☒	A full description of the statistical parameters including central tendency (e.g. means) or other basic estimates (e.g. regression coefficient) AND variation (e.g. standard deviation) or associated estimates of uncertainty (e.g. confidence intervals)
☐	☒	For null hypothesis testing, the test statistic (e.g. F, t, r) with confidence intervals, effect sizes, degrees of freedom and P value noted *Give P values as exact values whenever suitable.*
☒	☐	For Bayesian analysis, information on the choice of priors and Markov chain Monte Carlo settings
☒	☐	For hierarchical and complex designs, identification of the appropriate level for tests and full reporting of outcomes
☒	☐	Estimates of effect sizes (e.g. Cohen's d, Pearson's r), indicating how they were calculated

Our web collection on statistics for biologists contains articles on many of the points above.

Software and code

Policy information about availability of computer code

Data collection	Flow cytometry software: FACSDiva 8.0.1, CytExpert 2.1.0.92. Western blot: Li-Cor Image Studio 2.1.10.
Data analysis	Flow cytometry data was analyzed with FlowJo 10 software (Treestar). R 3.5.0 was used to calculate growth rates by calculating the log of the absolute cell counts and performing linear regressions. Western blot data was analyzed with Image Studio 2.1.10 software (Li-Cor). Microsoft Excel for Mac version 15.31 was used for basic statistical analysis. Graphpad Prism 7 was used for plotting data and cubic spline fitting. Custom Matlab 2014a and R 3.5.0 code was used for simulations and parameter identification (available from the corresponding author on reasonable request).

For manuscripts utilizing custom algorithms or software that are central to the research but not yet described in published literature, software must be made available to editors/reviewers. We strongly encourage code deposition in a community repository (e.g. GitHub). See the Nature Research guidelines for submitting code & software for further information.

Data

Policy information about availability of data

All manuscripts must include a data availability statement. This statement should provide the following information, where applicable:
- Accession codes, unique identifiers, or web links for publicly available datasets
- A list of figures that have associated raw data
- A description of any restrictions on data availability

All relevant data are included as source data and/or are available from the corresponding author on reasonable request. Plasmid sequences are deposited in GenBank under the accession codes MK775703-MK775710. Strains and plasmids used in this study are available from the corresponding author on reasonable request.

Field-specific reporting

Please select the one below that is the best fit for your research. If you are not sure, read the appropriate sections before making your selection.

☒ Life sciences   ☐ Behavioural & social sciences   ☐ Ecological, evolutionary & environmental sciences

For a reference copy of the document with all sections, see nature.com/documents/nr-reporting-summary-flat.pdf

Life sciences study design

All studies must disclose on these points even when the disclosure is negative.

Sample size	Each experiment was performed at least three times and is on par with standard bacterial experiments reported in the field.
Data exclusions	No data were excluded from analysis.
Replication	A minimum of three biological replicates were used and are indicated in the figure legends. All findings were reliably reproducible.
Randomization	Bacterial cultures were propagated from isogenic stocks derived from randomly selected colonies. When splitting cultures into different conditions as well as sampling cultures for measurements, cells within the cultures are randomly sampled as there is no control over which cells are selected.
Blinding	Researchers were not blinded during experiments because the experiments were not based on qualitative scoring metrics. In addition, each bacterial culture measurement is a random sampling of cells within a culture with no selection bias.

Reporting for specific materials, systems and methods

We require information from authors about some types of materials, experimental systems and methods used in many studies. Here, indicate whether each material, system or method listed is relevant to your study. If you are not sure if a list item applies to your research, read the appropriate section before selecting a response.

Materials & experimental systems

n/a	Involved in the study
☐	☒ Antibodies
☒	☐ Eukaryotic cell lines
☒	☐ Palaeontology
☒	☐ Animals and other organisms
☒	☐ Human research participants
☒	☐ Clinical data

Methods

n/a	Involved in the study
☒	☐ ChIP-seq
☐	☒ Flow cytometry
☒	☐ MRI-based neuroimaging

Antibodies

Antibodies used	Mouse anti-V5 tag primary antibody [E10] (AB53418, Abcam) at a 1:5,000 dilution, Goat anti-Mouse IRDye 800CW secondary antibody (925-32210, Li-Cor) was used at a 1:10,000 dilution.
Validation	Mouse anti-V5 tag primary antibody [E10] (AB53418, Abcam) was validated by the manufacturer for species-independent use for Western blots (https://www.abcam.com/v5-tag-antibody-e10-ab53418.html). Primary antibody specificity was also verified by the absence of signal in the Western blot of a V5-null E. coli lysate (See Extended Data Figure 5c, neg. ctrl.).

Flow Cytometry

Plots

Confirm that:

☒ The axis labels state the marker and fluorochrome used (e.g. CD4-FITC).

☒ The axis scales are clearly visible. Include numbers along axes only for bottom left plot of group (a 'group' is an analysis of identical markers).

☒ All plots are contour plots with outliers or pseudocolor plots.

☒ A numerical value for number of cells or percentage (with statistics) is provided.

Methodology

Sample preparation	Fluorescence measurements: Cells grown in minimal media were sampled and immediately read undiluted on the flow cytometer. Absolute cell count measurements: 75 μl samples of cells grown in methionine-dropout media were mixed with 79 μl of 500 μg/ml rifampicin in phosphate-buffered saline and 21 μl of 2 μm AccuCount Blank Particles (Spherotech) before being measured on a flow cytometer.
Instrument	The samples from the high throughput titrations in 96-well plates were analyzed on a LSRII Fortessa flow cytometer (BD Biosciences) equipped with a high throughput sampler. sfGFP was measured with a 488 nm laser and 530/30 and 505 LP emission filters; the voltage gains of the instrument were set as follows: forward scatter 500 V, side scatter 300 V, sfGFP 900 V. A minimum of 5,000 events were collected for each well using thresholds of 500 FSC-H and 500 SSC-H. Fluorescence measurements for the immunoblot lysate preparation cultures, step responses, steady-state negative perturbation, and absolute cell count measurements for the growth rate control experiments were performed using a CytoFlex S flow cytometer (Beckman Coulter) with a 488 nm laser and 525/40 BP filter; the gain settings of the instrument were as follows: forward scatter 100, side scatter 100, sfGFP 500. Thresholds of 2,500 FSC-H and 1,000 SSC-H were used for all samples. 50,000 events were collected for the lysate preparation, step response experiments, and steady-state disturbance rejection experiments and 1,000 AccuCount Blank Particles were collected for the growth rate control experiments..
Software	LSRII Fortessa data was collected with FACSDiva 8.0.1 software. CytoFlex S data was collected with CytExpert 2.1.0.92 software. FlowJo 10 (Treestar) was used for data analysis.
Cell population abundance	No cell sorting was performed.
Gating strategy	For fluorescence measurements, cells were initially separated from particles that were too small to be living bacterial cells using forward and side scatter thresholds (LSRII Fortessa: 500 FSC-H/500 SSC-H; CytoFlex S: 2,500 FSC-H/1,000 SSC-H). This population was further gated to exclude particles too small and too large to be single cells based on side-scatter (SSC-H) vs forward scatter (FSC-H) and side scatter (SSC-H) vs width (SSC-width). For absolute cell count measurements, cells and beads were initially separated from particles that were too small to be living bacterial cells or beads using forward and side scatter thresholds (CytoFlex S: 2,500 FSC-H/1,000 SSC-H). This population was further gated for cells based on side-scatter (SSC-H) vs forward scatter (FSC-H) and beads based on side-scatter (SSC-H) vs forward scatter (FSC-H).

☒ Tick this box to confirm that a figure exemplifying the gating strategy is provided in the Supplementary Information.